# A discrete λ-medial axis

John Chaussard, Michel Couprie and Hugues Talbot

Université Paris-Est, LIGM, Équipe A3SI, ESIEE Paris, France
e-mail: (j.chaussard,m.couprie,h.talbot)@esiee.fr

**Abstract.** The λ-medial axis was introduced in 2005 by Chazal and Lieutier as a new concept for computing the medial axis of a shape subject to filtering with a single parameter. These authors proved the stability of the λ-medial axis under small shape perturbations. In this paper, we introduce the definition of a discrete λ-medial axis (DLMA). We evaluate its stability and rotation invariance experimentally. The DLMA may be computed by efficient algorithms, furthermore we introduce a variant of the DLMA, denoted by DL'MA, which may be computed in linear-time. We compare the DLMA and the DL'MA with the recently introduced integer medial axis and show that both DLMA and DL'MA provide measurably better results.

In the 60s, Blum [7, 8] introduced the notion of medial axis or skeleton, which has since been the subject of numerous theoretical studies and has also proved its usefulness in practical applications. Although initially introduced as the outcome of a propagation process, the medial axis can also be defined in simple geometric terms. In the continuous Euclidean space, the two following definitions can be used to formalize this notion: let $X$ be a bounded subset of $\mathbb{R}^n$ ;

a) The skeleton of $X$ consists of the centers of the balls that are included in $X$ but that are not included in any other ball included in $X$.

b) The medial axis of $X$ consists of the points $x \in X$ that have several nearest points on the boundary of $X$.

The skeleton and the medial axis differ only by a negligible set of points (see [22]), in general the skeleton is a strict subset of the medial axis.

In this paper, we focus on medial axes in the discrete grid $\mathbb{Z}^2$ or $\mathbb{Z}^3$, which are centered in the shape with respect to the Euclidean distance.

A major difficulty when using the medial axis in applications (*e.g.*, shape recognition), is its sensitivity to small contour perturbations, in other words, its lack of stability. A recent survey [1] summarizes selected relevant studies dealing with this topic. This difficulty can be expressed mathematically: the transformation which associates a shape to its medial axis is only semi-continuous. This fact, among others, explains why it is usually necessary to add a filtering step (or pruning step) to any method that aims at computing the medial axis.

Hence, there is a rich literature devoted to skeleton or medial axis pruning, in which different criteria were proposed in order to discard "spurious" skeleton

points or branches: see $[4, 24, 3, 21, 2, 27, 17, 5, 13]$, to cite only a few. However, we lack theoretical justification, that is, a formalized argument that would help to understand why a filtering criterion is better than another.

In 2005, Chazal and Lieutier introduced the $\lambda$-medial axis and studied its properties, in particular those related to stability [9]. Consider a bounded subset $X$ of $\mathbb{R}^n$, as for example, for $n = 2$, the region enclosed by the solid curve depicted in Fig. 1 (left). Let $x$ be a point in $X$, we denote by $\Pi(x)$ the set of points of the boundary of $X$ that are closest to $x$. For example in Fig. 1, we have $\Pi(x) = \{a, b\}$, $\Pi(x') = \{a', b'\}$ and $\Pi(x'') = \{a''\}$. Let $\lambda$ be a non-negative real number, the $\lambda$-medial axis of $X$ is the set of points $x$ of $X$ such that the smallest ball including $\Pi(x)$ has a radius greater than or equal to $\lambda$. Notice that the 0-medial axis of $X$ is equal to $X$, and that any $\lambda$-medial axis with $\lambda > 0$ is included in the medial axis according to definition b). We show in Fig. 1 (right) two $\lambda$-medial axes with different values of $\lambda$.

A major outcome of [9] is the following property: informally, for "regular" values of $\lambda$, the $\lambda$-medial axis remains stable under perturbations of $\overline{X}$ that are small with regard to the Hausdorff distance. Typical non-regular values are radii of locally largest maximal balls.
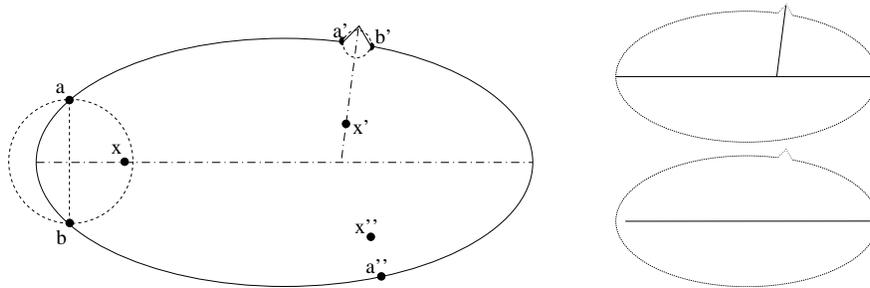


**Fig. 1.** Illustration of the $\lambda$-medial axis. Left: Points $x, x'$ and $x''$ and their respective closest boundary points. Top right: $\lambda$-medial axis with $\lambda = \epsilon$, a very small positive real number. Bottom right: $\lambda$-medial axis with $\lambda = d(a', b') + \epsilon$.

This property is a strong argument in favor of the $\lambda$-medial axis, especially in the absence of such result for other proposed criteria.

In the discrete grids, namely $\mathbb{Z}^2$ and $\mathbb{Z}^3$, a similar filtering criterion has been considered in independent works [21, 17]. It consists of selecting for each medial axis point only two closest boundary points, and using the distance between these two points as the filtering criterion. The work of Hesselink *et al.* [17] provides a linear-time algorithm to compute a filtered medial axis based on this criterion, which exhibits good noise robustness properties in practice.

In this paper, we introduce the definition of a discrete $\lambda$-medial axis (DLMA) in $\mathbb{Z}^n$. We evaluate experimentally its stability and rotation invariance in 2D. In this experimental study, we compare it with the previously introduced integer medial axis [18, 17] and show that the DLMA provides measurably better results. Furthermore, we introduce a variant of the DLMA which may be computed in

linear time, for which the results are very close to those of the DLMA, and which is only slightly slower than the one proposed in [17].

# 1 Discrete $\lambda$-medial axis

Let $x = (x_1, \ldots, x_n), y = (y_1, \ldots, y_n) \in \mathbb{R}^n$, we denote by $d(x, y)$ the Euclidean distance between $x$ and $y$, that is, $d(x, y) = (\sum_{k=1}^{n} (y_k - x_k)^2)^{\frac{1}{2}}$. Let $X$ be a finite subset of $\mathbb{R}^n$ or $\mathbb{Z}^n$. We set $d(y, X) = \min_{x \in X} \{d(y, x)\}$. We denote by $|X|$ the number of elements of $X$, and by $\overline{X}$ the complement of $X$.

Let $E$ be either $\mathbb{R}^n$ or $\mathbb{Z}^n$. Let $x \in E, r \in \mathbb{R}^+$, we denote by $B_r(x)$ the *ball of radius $r$ centered on $x$*, defined by $B_r(x) = \{y \in E \mid d(x, y) \leq r\}$. We also define $B_r^<(x) = \{y \in E \mid d(x, y) < r\}$.

For each point $x \in \mathbb{Z}^n$, we define the *direct neighborhood of $x$* as $N(x) = \{y \in \mathbb{Z}^n \mid d(x, y) \leq 1\}$. The direct neighborhood comprises $2n + 1$ points.

Let $S$ be a nonempty subset of $E$, and let $x \in E$. The *projection of $x$ on $S$*, denoted by $\Pi_S(x)$, is the set of points $y$ of $S$ which are at minimal distance from $x$ ; more precisely,
$$\Pi_S(x) = \{y \in S \mid \forall z \in S, d(y, x) \leq d(z, x)\}.$$
If $X$ is a subset of $E$, the *projection of $X$ on $S$* is defined by $\Pi_S(X) = \bigcup_{x \in X} \Pi_S(x)$.

In the case of a subset $X$ of $\mathbb{Z}^n$, it may be easily seen that $\Pi_{\overline{X}}(X)$ is composed of the points of $\overline{X}$ that are in the direct neighborhood of a point of $X$, that is, $\Pi_{\overline{X}}(X) = \{y \in \overline{X} \mid N(y) \cap X \neq \emptyset\}$. We call $\Pi_{\overline{X}}(X)$ the *(external) boundary of $X$*.

Let $S \subset \mathbb{R}^n$, we denote by $R(S)$ the radius of the smallest ball enclosing $S$, that is, $R(S) = \min\{r \in \mathbb{R} \mid \exists y \in \mathbb{R}^n, B_r(y) \supseteq S\}$.

The $\lambda$-medial axis may now be defined based on these notions.

**Definition 1** ([9]). *Let $X$ be an open bounded subset of $\mathbb{R}^n$, and let $\lambda \in \mathbb{R}^+$. The $\lambda$-medial axis of $X$ is the set of points $x$ in $X$ such that $R(\Pi_{\overline{X}}(x)) \geq \lambda$.*

We cannot transpose this definition straightforwardly to $\mathbb{Z}^n$. To see why, consider a horizontal ribbon in $\mathbb{Z}^2$ with constant even width and infinite length. It can be seen that any point of this set has a projection that is reduced to a singleton. Hence, if we keep the same definition, any $\lambda$-medial axis of this object with $\lambda > 0$ would be empty.

It is the reason why we change the projection for the extended projection (see [13]).

Let $X \subseteq \mathbb{Z}^n$, and let $x \in X$. The *extended projection of $x$ on $\overline{X}$*, denoted by $\Pi_{\overline{X}}^e(x)$, is the union of the sets $\Pi_{\overline{X}}(y)$, for all $y$ in $N(x)$ such that $d(y, \overline{X}) \leq d(x, \overline{X})$.

The last condition ($d(y, \overline{X}) \leq d(x, \overline{X})$) is set in order to avoid getting several medial axis points when only one is sufficient. We are now ready to introduce the definition of our discrete $\lambda$-medial axis.

**Definition 2.** *Let $X$ be a finite subset of $\mathbb{Z}^n$, and let $\lambda \in \mathbb{R}^+$. We define the function $\mathcal{F}_X$ which associates, to each point $x$ of $X$, the value $\mathcal{F}_X(x) = R(\Pi_{\overline{X}}^e(x))$. The discrete $\lambda$-medial axis (or DLMA) of $X$ is the set of points $x$ in $X$ such that $\mathcal{F}_X(x) \geq \lambda$.*

In Fig. 2 (right), we show two examples of DLMAs of a shape $X$. We also note that the function $\mathcal{F}_X$ (displayed on the left of the figure) can be computed once and stored as a grayscale image, and that any DLMA of $X$ is a threshold of this function at a particular value $\lambda$. More examples are given in Fig. 3. Notice that DLMA has not, in general, the same topology as the original shape.
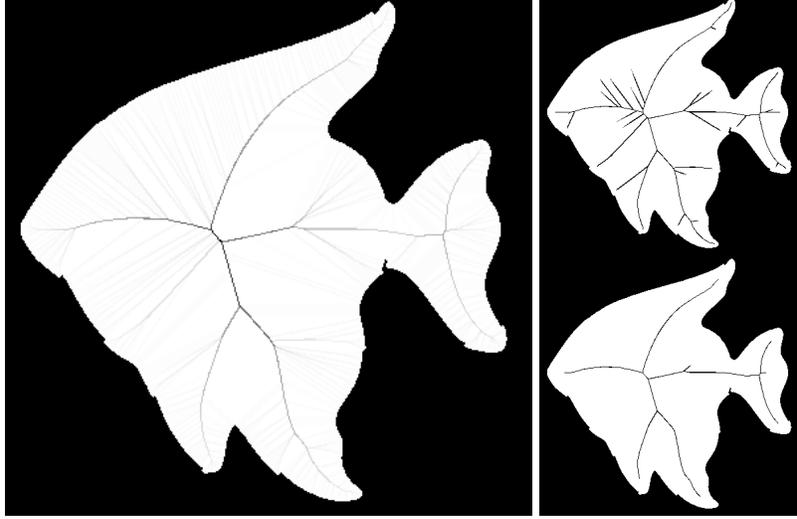


**Fig. 2.** Left: The function $\mathcal{F}_X$ superimposed to the shape $X$. Darkest colors represent highest values of $\mathcal{F}_X(x)$. Any DLMA of $X$ is a threshold of this function at a particular value $\lambda$. Top right: discrete 10-medial axis. Bottom right: discrete 30-medial axis of $X$.

## 2 Integer medial axis

Let us first recall the definition of the integer medial axis [17], which is conceptually close to the DLMA, and defined in the same framework of discrete grids.

Let $X$ be a subset of $\mathbb{Z}^n$, and let $x \in X$. We denote by $\Pi'_{\overline{X}}(x)$ the element of $\Pi_{\overline{X}}(x)$ that is smallest with regard to the lexicographic ordering of its coordinates.

**Definition 3** ([17]). *Let $X$ be a finite subset of $\mathbb{Z}^n$, and let $\gamma \in \mathbb{R}^+$. The $\gamma$-integer medial axis (or GIMA) of $X$ is the set of points $x$ in $X$ such that*
*i) $\exists y \in N(x)$, $d(\Pi'_{\overline{X}}(x), \Pi'_{\overline{X}}(y)) > \gamma$, and*
*ii) $d(m - \Pi'_{\overline{X}}(x)) \leq d(m - \Pi'_{\overline{X}}(y))$, where $m = \frac{x+y}{2}$.*
*The* integer medial axis of $X$ *is the $\gamma$-integer medial axis of $X$ for $\gamma = 1$.*

Notice that the GIMA is not invariant under a permutation of the coordinates.

There are indeed some links between the GIMA and the DLMA. In 2D, in the case of a point $x$ that is, conceptually, a "regular skeleton point" (neither a

branch extremity nor a branch junction), condition i) is similar to the condition $R(\Pi_{\overline{X}}(x)) \geq \lambda$ in Def. 1.

Condition ii) plays a role analogous to condition $d(y, \overline{X}) \leq d(x, \overline{X})$ in the definition of the extended projection, that is to get a thinner axis.

However, these definitions differ, leading to sensible differences in the results of these two transformations (see Fig. 3). We analyse quantitatively these differences in Sec. 5.
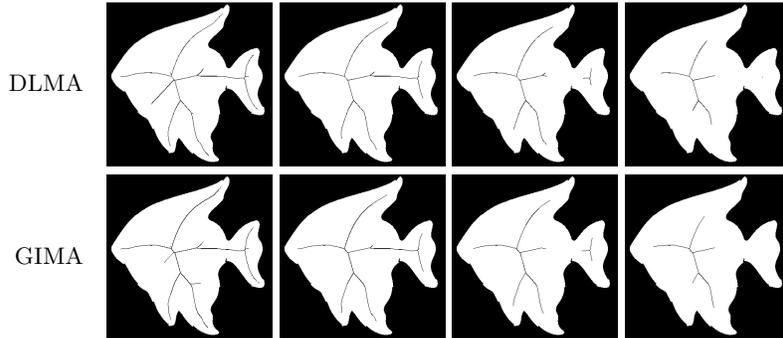


**Fig. 3.** Results of DLMA (first row) and GIMA (second row) for parameter values yielding similar reconstruction ratios (see Sec. 5).

## 3 Topology preservation

It is easy to see that a DLMA or a GIMA of a given shape $X$ does not exhibit, in general, the same homotopy type as $X$ (see *e.g.* Fig. 3).

In order to guarantee topology preservation, a popular method [14, 29, 28, 25] consists of performing a homotopic thinning of $X$ with the constraint of retaining the points of its filtered medial axis $M$, or equivalently, of iteratively removing simple points [19, 6, 12] from $X$ that do not belong to $M$. A priority function is needed in order to specify which points must be considered at each step of the thinning. In the general case, the choice of this priority function is not easy (see [28, 13]). In the case of a DLMA, choosing the map $\mathcal{F}_X$ as priority function yields satisfying results (see, for example, Fig. 4).

## 4 Algorithms

The projection $\Pi_{\overline{X}}(x)$, for all points $x$ in $X$, can be computed in optimal time and space (that is, in $O(N)$ where $N = \sum_{x \in X} |\Pi_{\overline{X}}(x)|$) thanks to an algorithm due to D. Coeurjolly [13].

In order to avoid computing the map $\Pi_{\overline{X}}$, which requires a data structure like an array of lists to store all the sets $\Pi_{\overline{X}}(x)$, we propose a variant of the
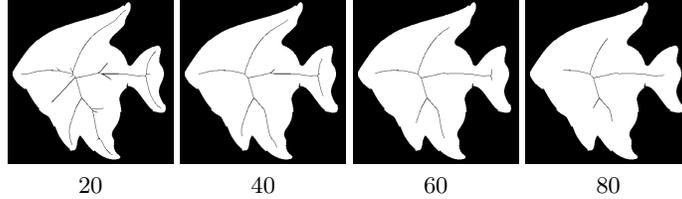
**Fig. 4.** Results of homotopic thinning of $X$ constrained by the DLMA for parameter values 20, 40, 60 and 80, and with $\mathcal{F}_X$ as priority function.

DLMA that consists of replacing $\Pi_{\overline{X}}$ by $\Pi'_{\overline{X}}$ in the definition of the extended projection. We will refer to this variant as the discrete $\lambda'$-medial axis (DL'MA). Notice that the DL'MA, as the GIMA, is not invariant under a permutation of the coordinates. In our experiments (see Sec. 5), we tried both variants and found very little difference between their results. One advantage of this variant is that the map $\Pi'_{\overline{X}}$ can be computed in linear time and stored in an array of integers [10, 23, 17].

The smallest ball enclosing a given set of $n$ points in $\mathbb{R}^d$ can be computed in expected $O(n)$ time if $d$ is considered as a constant, thanks to an algorithm due to Welzl [30]. This algorithm is simple and easy to implement (see appendix).

For each object point $x$, the computational cost is in $O(n)$ where $n = |\Pi^e_{\overline{X}}(x)|$ (see Def. 2). In the variant DL'MA, we have $n \leq 5$, since only one projection point is considered for $x$ and, at worse, each of its four direct neighbors. Hence, computing the radius of the smallest enclosing ball can be performed in constant time.

Globally, the DL'MA procedure runs in linear time with regard to the number of object points.

Thanks to local characterizations, in 2D and 3D, checking whether a point is simple or not can be done in constant time. The homotopic thinning described in section 3 may be implemented to run in $O(n \log n)$ complexity, where $n$ is the number of object points, using *e.g.* a balanced binary tree to store and retrieve the candidate points and their priority.

## 5   Results and comparisons

First, let us give some definitions that are useful for describing our experiments and analyzing their results.

Let $X$ be a finite subset of $\mathbb{Z}^n$. Let $Y$ be a subset of $X$, we set $REDT_X(Y) = \bigcup_{y \in Y} B^<_{d(y, \overline{X})}(y)$. The transformation $REDT_X$ is sometimes called *reverse Euclidean distance transform* [11].

It is well known that any object can be fully reconstructed from its medial axis, more precisely, we have $X = REDT_X(M)$ whenever $M$ is the (exact and non-filtered) medial axis of $X$. This property holds if $M$ is the set of the centers of maximal balls of $X$, the DLMA of $X$ with $\lambda = 1$, or the integer medial axis of $X$. However, it is no longer true if we consider filtered medial axes, *e.g.* DLMA or GIMA with arbitrary $\lambda$ or $\gamma$.

Then, it is interesting to measure how much information about the original object is lost when we raise the filtering parameter. We set

$$\mathcal{L}_X(\lambda) = \frac{|X \setminus REDT_X(LM_X(\lambda))|}{|X|}, \quad \mathcal{I}_X(\gamma) = \frac{|X \setminus REDT_X(IM_X(\gamma))|}{|X|},$$

where $LM_X(\lambda)$ is the DLMA of $X$ and $IM_X(\gamma)$ is the GIMA of $X$. In words, $\mathcal{L}_X(\lambda)$ (resp. $\mathcal{I}_X(\gamma)$) is the area of the difference between $X$ and the set reconstructed from its DLMA (resp. GIMA), divided by the area of $X$. We call $\mathcal{L}_X(\lambda)$ and $\mathcal{I}_X(\gamma)$ the *(normalized) residuals* corresponding to filtering values $\lambda$ and $\gamma$, respectively.

Fig. 5 shows the evolution of the residuals for the GIMA, DLMA and DL'MA. Since some differences may not be negligible, to ensure a fair evaluation we will compare the results of both methods for approximately equal values of their residuals, rather than for equal values of their parameters.
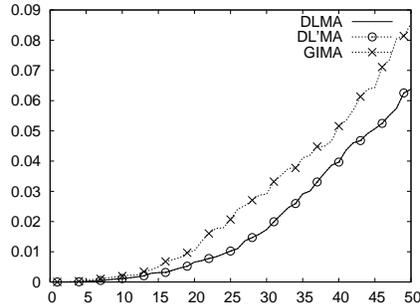


**Fig. 5.** Residuals $\mathcal{L}_X(\lambda)$ (2 variants) and $\mathcal{I}_X(\gamma)$, for the set $X$ depicted in Fig. 2. Horizontal axis: the value of the parameter ($\lambda$ or $\gamma$). Vertical axis: the value of the residual. Notice that curves corresponding to DLMA and DL'MA are superimposed.

For comparing shapes or medial axes, we use the Hausdorff distance (see below), and also a dissimilarity measure proposed by Dubuisson and Jain [15]. The drawback of Hausdorff distance for measuring shape dissimilarity is its extreme sensibility to outliers, the latter measure avoids this drawback.

Let $X, Y$ be two subsets of $\mathbb{R}^n$. We set

$$H(X|Y) = \max_{x \in X}\{\min_{y \in Y}\{d(x,y)\}\},$$

and $d_H(X,Y) = \max\{H(X|Y), H(Y|X)\}$ is the *Hausdorff distance between $X$ and $Y$*. We set

$$D(X|Y) = \frac{1}{|X|} \sum_{x \in X} \min_{y \in Y}\{d(x,y)\},$$

and $d_D(X,Y) = \max\{D(X|Y), D(Y|X)\}$ is the *Dubuisson and Jain's dissimilarity measure between $X$ and $Y$* (called *dissimilarity* in the sequel for the sake of brevity).

We conducted our experiments on a database of 216 shapes provided by B.B. Kimia [26]. The 216 images are divided into 18 classes (birds, cars, etc.), Fig. 6 shows one (reduced) image of each class.
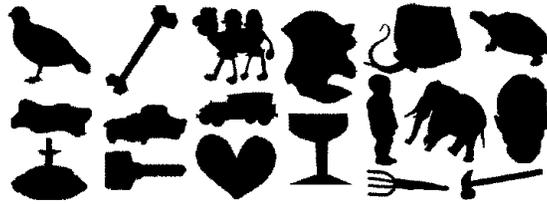


**Fig. 6.** A sample of the 216 shapes of Kimia's database.

### 5.1 Stability

Skeletons are notoriously sensitive to border noise. Since the $\lambda$-medial axis is supposed to cope reasonably well with shape deformation, it is useful to test how it fares in practice.

To introduce noise to the boundary of an object we propose deforming it using a process derived from the Eden accretion process [16]. The Eden process is an iterative random cellular automaton which, in its simplest form, attributes an equal probability to all the outer border points to be set to 1 at each step. That is, at each step, a neighbour of the object is chosen randomly and added to the shape. In spite of its simplicity, the Eden process exhibits good asymptotic isotropy [20]. In our process, we combined an Eden step of accretion with an opposite step of reduction, where a random pixel belonging to the inner border is turned to zero (i.e. set to belong to the background). In addition, we required both accretion and diluvion steps to concern only simple points. This way at each step the object's area remains constant and retains the homotopy type of the original.

We denote by $E(X, n)$ the result of applying $n$ steps of this process to the shape $X$. In this experiment, we compare the (filtered) medial axis of an original shape with the one of a deformed shape.
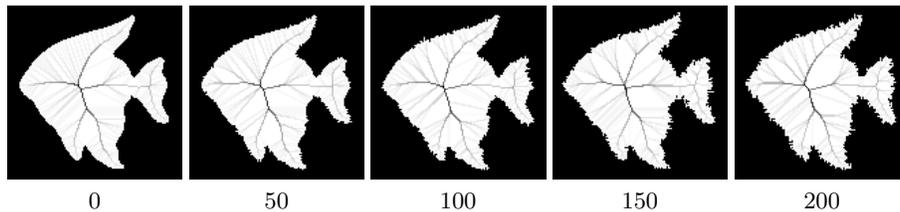


| 0 | 50 | 100 | 150 | 200 |

**Fig. 7.** Illustration of the border deformation process, after 0 (original image), 50, 100, 150 and 200 steps. The function $\mathcal{F}_X$ is superimposed to each shape $X$.

|       | 50   | 100  | 150  | 200  | all  |
|-------|------|------|------|------|------|
| GIMA  | 5.52 | 6.58 | 7.09 | 7.59 | 6.70 |
| DLMA  | 5.37 | 6.31 | 6.81 | 7.32 | 6.45 |
| DL'MA | 5.35 | 6.32 | 6.79 | 7.32 | 6.45 |

**Table 1.** Hausdorff distance.

|       | 50   | 100  | 150  | 200   | all  |
|-------|------|------|------|-------|------|
| GIMA  | .551 | .772 | .889 | 1.016 | .807 |
| DLMA  | .547 | .763 | .881 | .998  | .797 |
| DL'MA | .551 | .768 | .885 | 1.004 | .802 |

**Table 2.** Dissimilarity.

In Table 1 (resp. Table 2) we give the average Hausdorff distance (resp. dissimilarity) between $M(X)$ and $M(E(X, n))$ on the 216 shapes of Kimia's database, for parameter values $\gamma, \lambda, \lambda'$ varying from 1 to a value giving 30% residual. Results are given for values 50, 100, 150, 200 of $n$ and all results averaged together. Results indicate a slight advantage of $\lambda$- and $\lambda'$-medial axes over the integer medial axis.

### 5.2 Rotation invariance

Rotation invariance is an important property of the medial axis that holds in the continuous framework. If $R_\theta$ denotes the rotation of angle $\theta$ and center 0, and $M$ denotes the medial axis transform, the rotation invariance property states that $M(R_\theta(X)) = R_\theta(M(X))$, whatever $X$ and $\theta$.

In a discrete framework, this property can only hold for particular cases (*e.g.*, when $\theta$ is a multiple of 90 degrees). Nevertheless, we can experimentally measure the dissimilarity between $M(R_\theta(X))$ and $R_\theta(M(X))$ for different instances, and different definitions of the medial axis. The lower this dissimilarity, the more stable under rotation the method is.

Fig. 8 and Fig. 9 show detailed results of such experiments. We used a rotation by interpolation algorithm, followed by a threshold. We adjusted the parameters $\lambda$ and $\gamma$ such that the residuals for each axis were approximately 1%, 3% and 5%.
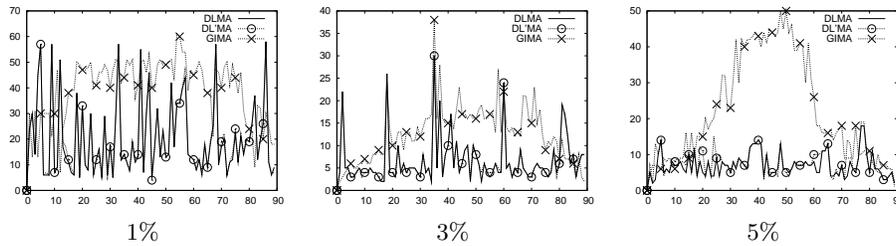


**Fig. 8.** Hausdorff distance between $M(R_\theta(X))$ and $R_\theta(M(X))$, for residual values 1%, 3%, 5%. Horizontal axis: $\theta$. Vertical axis: Hausdorff distance.

For each shape of Kimia's database, we computed the Hausdorff distance and the dissimilarity between $M(R_\theta(X))$ and $R_\theta(M(X))$ for values of the parameters
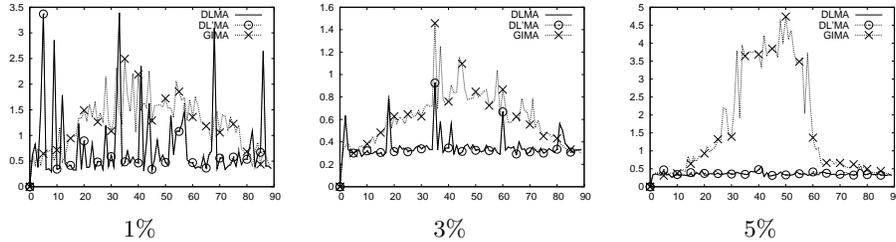
**Fig. 9.** Dissimilarity between $M(R_\theta(X))$ and $R_\theta(M(X))$, for residual values 1%, 3%, 5%. Horizontal axis: $\theta$. Vertical axis: Dissimilarity.

yielding 1%, 2%, 3%, 4%, 5% and 6% residuals, and for rotation angles varying from 0 to 89 degrees by 1 degree steps.

The results are summarized in Tables 3 and 4. In Table 3 (resp. Table 4) we give the average Hausdorff distance (resp. dissimilarity) between $M(R_\theta(X))$ and $R_\theta(M(X))$ on the 216 shapes of Kimia's database, for $\theta$ varying from 0 to 89 degrees, and for residual values 1%, 2%, 3%, 4%, 5%, 6% and all values together. We see that the average dissimilarity or Hausdorff distance is almost always less for the DLMA (or DL'MA) than for the integer medial axis, around 15% less in the mean. The difference between both methods is more important (greater than 20%) for parameter values yielding highest residuals.

|        | 2%   | 4%   | 6%   | all  |
|--------|------|------|------|------|
| GIMA   | 6.76 | 6.59 | 7.34 | 6.94 |
| DLMA   | 6.17 | 5.48 | 5.71 | 6.03 |
| DL'MA  | 6.17 | 5.43 | 5.71 | 5.99 |

**Table 3.** Hausdorff distance.

|        | 2%   | 4%   | 6%   | all  |
|--------|------|------|------|------|
| GIMA   | .620 | .628 | .796 | .677 |
| DLMA   | .563 | .480 | .580 | .559 |
| DL'MA  | .566 | .479 | .602 | .557 |

**Table 4.** Dissimilarity.

### 5.3 Computing time

In Fig. 10, we show the results of computing time measurements that we performed on an Intel Core 2 Duo processor at 1.83 GHz. Computing times for the GIMA are the lowest, but DL'MA is only slightly slower (and also linear).

## 6 Conclusion

In this paper, we introduced the definition of a discrete $\lambda$-medial axis (DLMA) and compared it with the integer medial axis. We showed the DMLA provides good robustness to boundary noise and invariance by rotation in practice. We proposed an improved DM'LA algorithm with linear complexity. Future work will include a more thorough study of rotational invariance and border noise robustness, both in 2D and 3D, including comparison with traditional pruning. We will also study in more details the relationship of the DLMA to the discrete bisector function [28, 13] and application of this work to shape classification and object splitting.
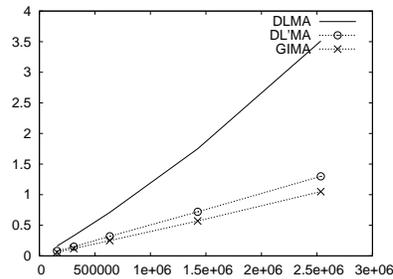
**Fig. 10.** Computing times (in seconds, vert. axis) versus image sizes (horiz. axis).

## References

1. D. Attali, J.-D. Boissonnat, and H. Edelsbrunner. Stability and computation of the medial axis — a state-of-the-art report. In *Mathematical Foundations of Scientific Visualization, Computer Graphics, and Massive Data Exploration*, pages 1–19. Springer-Verlag, 2009. to appear.
2. D. Attali and J.O. Lachaud. Delaunay conforming iso-surface, skeleton extraction and noise removal. *Comp. Geom.: Theory and Applications*, 19:175–189, 2001.
3. D. Attali and A. Montanvert. Modelling noise for a better simplification of skeletons. In *ICIP*, volume 3, pages 13–16, 1996.
4. D. Attali, G. Sanniti di Baja, and E. Thiel. Pruning discrete and semicontinuous skeletons. In *Conf. Im. Analysis and Processing*, volume 974 of *LNCS*, pages 488–493. Springer, 1995.
5. X. Bai, L.J. Latecki, and W.Y. Liu. Skeleton pruning by contour partitioning with discrete curve evolution. *Trans. on PAMI*, 29(3):449–462, 2007.
6. G. Bertrand. Simple points, topological numbers and geodesic neighborhoods in cubic grids. *Pattern Recognition Letters*, 15:1003–1011, 1994.
7. H. Blum. An associative machine for dealing with the visual field and some of its biological implications. *Biol. prototypes and synthetic systems*, 1:244–260, 1961.
8. H Blum. A transformation for extracting new descriptors of shape. In *Models for the Perception of Speech and Visual Form*, pages 362–380. MIT Press, 1967.
9. F. Chazal and A. Lieutier. The λ-medial axis. *Graph. Models*, 67(4):304–331, 2005.
10. D. Coeurjolly. *Algorithmique et géométrie discrète pour la caractérisation des courbes et des surfaces*. PhD thesis, Université Lyon II, France, 2002.
11. D. Coeurjolly. d-dimensional reverse Euclidean distance transformation and Euclidean medial axis extraction in optimal time. In *procs. DGCI, LNCS, Springer Verlag*, volume 2886, pages 327–337, 2003.
12. M. Couprie and G. Bertrand. New characterizations of simple points in 2D, 3D and 4D discrete spaces. *Trans. on PAMI*, 31(4):637–648, April 2009.
13. M. Couprie, D. Coeurjolly, and R. Zrour. Discrete bisector function and Euclidean skeleton in 2D and 3D. *Image and Vision Computing*, 25(10):1543–1556, 2007.
14. E.R. Davies and A.P.N. Plummer. Thinning algorithms: a critique and a new methodology. *Pattern Recognition*, 14:53–63, 1981.
15. M.-P. Dubuisson and A.K. Jain. A modified hausdorff distance for object matching. In *12th ICPR*, volume 1, pages 566–568, 1994.
16. M. Eden. A two-dimensional growth process. In *Fourth Berkeley Symp. on Math. Statist. and Prob.*, volume 4, pages 223–239. Univ. of Calif. Press, 1961.

17. W.H. Hesselink and J.B.T.M. Roerdink. Euclidean skeletons of digital image and volume data in linear time by the integer medial axis transform. *Trans. on PAMI*, 30(12):2204–2217, 2008.
18. W.H. Hesselink, M. Visser, and J.B.T.M. Roerdink. Euclidean skeletons of 3d data sets in linear time by the integer medial axis transform. In *7th ISMM*, volume 30 of *Computational Imaging and Vision*, pages 259–268. Springer, 2005.
19. T. Yung Kong and A. Rosenfeld. Digital topology: introduction and survey. *Comp. Vision, Graphics and Image Proc.*, 48:357–393, 1989.
20. T.M.C. Lee and R. Cowan. A stochastic tesselation of digital space. In *2nd ISMM*, pages 218–224, Fontainebleau, 1994. Kluwer.
21. G. Malandain and S. Fernández-Vidal. Euclidean skeletons. *Image and Vision Computing*, 16:317–327, 1998.
22. G. Matheron. *Examples of topological properties of skeletons*, volume 2, pages 217–238. Academic Press, 1988.
23. C.R. Maurer, R. Qi, and V. Raghavan. A linear time algorithm for computing exact euclidean distance transforms of binary images in arbitrary dimensions. *Trans. on PAMI*, 25(2):265–270, 2003.
24. R.L. Ogniewicz and O. Kübler. Hierarchic voronoi skeletons. *Pattern Recognition*, 28(33):343–359, 1995.
25. C. Pudney. Distance-ordered homotopic thinning: a skeletonization algorithm for 3D digital images. *Comp. Vision and Im. Understanding*, 72(3):404–413, 1998.
26. D. Sharvit, J. Chan, H. Tek, and B.B. Kimia. Symmetry-based indexing of image databases. *J. of Visual Comm. and Im. Representation*, 9(4):366–380, 1998.
27. S. Svensson and G. Sanniti di Baja. Simplifying curve skeletons in volume images. *Comp. Vision and Im. Understanding*, 90(3):242–257, 2003.
28. H. Talbot and L. Vincent. Euclidean skeletons and conditional bisectors. In *VCIP'92, SPIE*, volume 1818, pages 862–876, 1992.
29. L. Vincent. Efficient computation of various types of skeletons. In *Medical Imaging V, SPIE*, volume 1445, pages 297–311, 1991.
30. E. Welzl. Smallest enclosing disks (balls and ellipsoids). In *Results and New Trends in Computer Science*, volume 555 of *LNCS*, pages 359–370. Springer-Verlag, 1991.

## Appendix

The following recursive function, introduced and analyzed in [30], computes the smallest ball enclosing the set of points $P$, and having the points of the set $R$ on its boundary. The initial call is done with $R = \emptyset$. The result $B$ is made of the center and the radius of the enclosing ball.

---

**Algorithm 1**: Function SmallestEnclosingBall($P, R$)

---
**Data** : $P \subseteq \mathbb{R}^d, R \subseteq \mathbb{R}^d$
**if** $P = \emptyset$ *[or $|R| = d + 1$]* **then** compute $B$ directly;
**else**
    choose $p \in P$ at random;
    $B$ = SmallestEnclosingBall($P \setminus \{p\}, R$);
    **if** *[B defined and]* $p \notin B$ **then** $B$ = SmallestEnclosingBall($P \setminus \{p\}, R \cup \{p\}$);
**return** $B$;

---